PHOTONICS Research

Control of the harmonic near-field distributions by an active metasurface loaded with pin diodes

Jin Yang,[1,†] Jun Chen Ke,[1,†] Mao Chen,[1,†] Ming Zheng Chen,[1] Jun Yan Dai,[1] Jian Feng Chen,[1] Rui Yang,[1] Jun Wei Wu,[1] Qiang Cheng,[1,*] and Tie Jun Cui[1,2]

[1]*State Key Laboratory of Millimeter Waves, Southeast University, Nanjing 210096, China*
[2]*e-mail: tjcui@seu.edu.cn*
Corresponding author: qiangcheng@seu.edu.cn

Recent advances of space-time-coding digital metasurfaces demonstrate powerful capabilities in the generation of nonlinear harmonics and the accurate control of the corresponding wavefronts. However, to date the near field manipulation and the experiment characterization are still not explored. In this paper, we propose a space-time-digital coding metasurface to realize accurate manipulation of the near fields at the fundamental and +1st (−1st) harmonics simultaneously, by properly controlling the initial phase and time delay of the time varying reflectivity. A novel mapping system is established to measure the nonlinear near field distributions of multiharmonics. Both the simulation and experimental results demonstrate the validity of the proposed method. © 2021 Chinese Laser Press

1. INTRODUCTION

Metasurfaces have attracted enormous interest due to their intriguing electromagnetic (EM) responses, which bring us many fascinating physical phenomena including negative refraction [1,2], perfect lensing [3], and invisibility cloaking [4–6]. The metasurfaces usually consist of the resonant or nonresonant subwavelength elements, whose reflection/transmission coefficients can be customized at will by changing the size, shape [7], or orientation of unit cells [8–10]. Due to the elaborate arrangement of the metaatoms across the whole metasurface, the phase discontinuities can be introduced to control the propagation direction [11], polarization state [12–14], and wavefront [15–19] of EM waves. To simplify the complexity of metasurface design, coding metasurfaces [20,21] were proposed to facilitate accurate control of the EM waves based on the coding sequences of binary metaatoms. Hence, versatile functionalities of the coding metasurfaces have been demonstrated, including ultrathin planar lenses [22,23], vortex beam generations [24–26], and metasurface holograms [27–30].

However, most of these metasurfaces are passive, and their functions are fixed once they have been fabricated. To overcome these limitations, dynamic control of the EM waves was proposed based on programmable/tunable metasurfaces. These metasurfaces are usually integrated with active devices, such as positive-intrinsic-negative (PIN) diodes [31–35], varactors [36–39], and microelectro-mechanical systems [40]. However, most of the aforementioned programmable metasurfaces only focus on the control of the incident carrier wave, but seldom realize accurate manipulations of nonlinear amplitudes and phases.

In the THz and visible regimes, plenty of metasurfaces were proposed to control nonlinear wave responses, including the intensity, phase, and the polarization state [41–45]. However, the simultaneous control of the harmonic amplitudes and phases still remains a great challenge. Recently, space-time-digital metasurfaces [46–50] were proposed to solve this problem. By dynamically altering the local amplitude or phase of the surface reflectivity in a periodic manner, the metasurfaces showed powerful capabilities in the generation and manipulation of a specific order harmonic [46–50]. Furthermore, Dai *et al.* proposed a method to realize independent control of two harmonics [51]. However, these works did not explore the simultaneous manipulation of the fundamental and high-order harmonics. Furthermore, recent studies on space-time digital metasurfaces were restricted to their far-field characteristics, but the nonlinear near-field manipulation is seldom investigated experimentally.

On this basis, we propose a scheme to realize the manipulation of the fundamental and high-order harmonics simultaneously via the space-time digital metasurface. A novel experimental platform for nonlinear field mapping is developed to monitor the harmonic near field distributions. As an example, we show the feasibility of achieving two symmetric beams at the fundamental frequency, and the orbital angular

momentum (OAM) beams with different topological numbers at ±1st order harmonics. The space-time digital metasurface is designed, fabricated, and measured at different harmonics. The experimental results validate the effectiveness of the theoretical analyses.

2. THEORY AND DESIGN

As shown in Fig. 1, the proposed space-time digital metasurface is composed of periodic metaatoms loaded with PIN diodes. By introducing initial phase φ_A and time delay t_1, the reflectivity $\Gamma_{pq}(t)$ of the element (p, q) in the metasurface can be defined as

$$\Gamma_{pq}(t) = \sum_{m=0}^{M-1} A\Gamma_m g(t - t_1 - m\tau), \quad 0 < |t| < T, \quad \text{(1)}$$

where $g(t)$ is basic pulse function with the modulation period $T = M \times \tau$. τ is the pulse width. M is the pulse number in a period. Γ_m is the reflectivity at the interval $(m - 1)\tau < t < m\tau$. A is a constant with $A = |A| \exp(j\varphi_A)$.

Under the monochromatic wave incidence $E_i(t) = \exp(j\omega_c t)$, the reflected spectrum is composed of many harmonics [46]. c_{pq}^k is defined as the complex Fourier coefficient of the periodic reflectivity $\Gamma_{pq}(t)$ at the kth order harmonic $\omega = k\omega_0 + \omega_c$, where $\omega_0 = 2\pi/T$, $k = 0, \pm 1, \pm 2, \pm 3, \cdots$. ω_0 and ω_c are the modulation frequency and the carrier frequency, respectively. c_{pq}^k can be written as

$$c_{pq}^k = |A| \exp[-j(k\omega_0 t_1 - \varphi_A)](a_{pq}^k). \quad \text{(2)}$$

Here, a_{pq}^k is presented as

$$a_{pq}^k = \frac{1}{M} Sa\left(\frac{k\pi}{M}\right) e^{-j\frac{k\pi}{M}} \sum_{n=0}^{M-1} \Gamma_n \exp(-jk\omega_0 m\tau). \quad \text{(3)}$$

The phase of the kth order harmonic can be

$$\varphi_{pq}^k = \arg(c_{pq}^k) = -(k\omega_0 t_1 - \varphi_A) + \varphi_{pq}^{*k}, \quad \text{(4)}$$

where $\varphi_{pq}^{*k} = \arg(a_{pq}^k)$. It depends on the pulse number and pulse amplitude simultaneously from Eq. (3).

In this study, we consider a high-efficiency reflective metasurface with $|\Gamma_m| = 1$. Two states, namely 0 and 1 states, are found with the reflection phases of $\Gamma_{pq}(t)$ to be 0° and 180°, respectively. From Eqs. (2) and (3), the duty cycle of the reflection phases of $\Gamma_{pq}(t)$ is very important for the energy conversion from the fundamental wave into the different harmonics. As an example, altogether 12 time slots with the duty cycle of 1/3 are selected to get the larger amplitudes for the 0th, −1st, 1st order harmonics. For simplicity, the basic coding sequence is chosen as 000011111111, implying that the reflection phases are 0° in the first four time slots, and 180° in the last eight time slots. The corresponding reflection amplitude and phase spectra can be found in Fig. 2(a), with $\varphi_A = 0°$ and $t_1 = 0$. However, as demonstrated in Figs. 2(b) and 2(c), the phases φ_A and time delays t_1 also show great influence on the harmonic phase distributions, which is consistent with the prediction from Eq. (4).

From Eq. (4), the harmonic phases for the fundamental and ±1st order harmonics are obtained as

$$\varphi_{pq}^0 = \varphi_A + \varphi_{pq}^{*0},$$
$$\varphi_{pq}^1 = \varphi_A - \omega_0 t_1 + \varphi_{pq}^{*1},$$
$$\varphi_{pq}^{-1} = \varphi_A + \omega_0 t_1 + \varphi_{pq}^{*-1}. \quad \text{(5)}$$

According to Eqs. (2)–(4) when the coding sequence Γ_m and period T are determined, φ_{pq}^{*0}, φ_{pq}^{*1}, and φ_{pq}^{*-1} are fixed. Thus, we control the phases of any two harmonics independently by
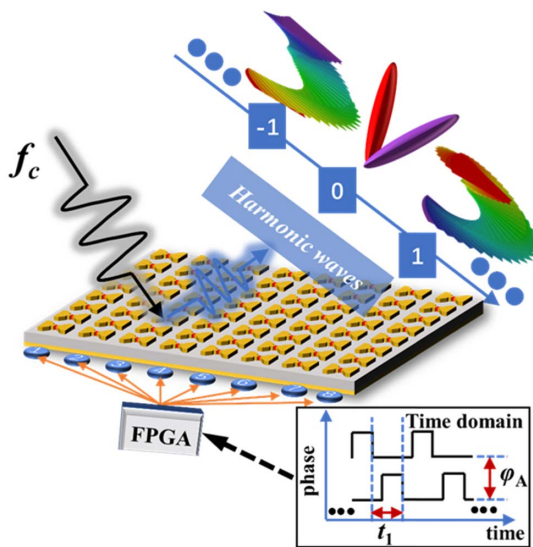

Fig. 1. Schematic of the space-time digital coding metasurface, which can independently control the wavefronts of the fundamental and high-order harmonics by adjusting the phase φ_A, and the time delay t_1 of the periodic reflectivity.
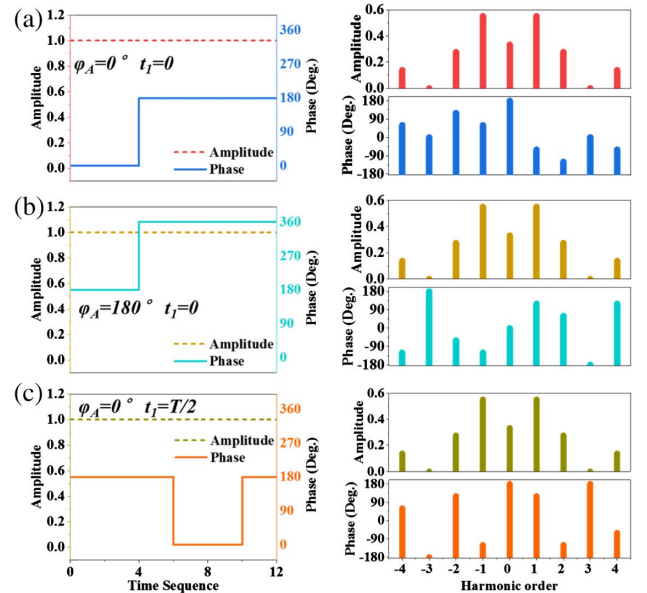

Fig. 2. Reflection amplitudes and phases of $\Gamma_{pq}(t)$ in each period (left column) and the calculated reflection spectra (right column) under different combinations of φ_A and t_1, when the coding sequence 000011111111 is employed. (a) $\varphi_A = 0°$, $t_1 = 0$, (b) $\varphi_A = 180°$, $t_1 = 0$, (c) $\varphi_A = 0°$, $t_1 = T/2$.

choosing the proper sets of (φ_A, t_1), which enables us to design and realize various functionalities at different harmonics.

To validate the concepts illustrated in Fig. 1, a metaatom in Fig. 3 is designed to achieve the time-varying reflectivity by switching the embedded PIN diode between the on and off states. It consists of two dielectric substrates. Two symmetrical metallic patches are connected by a PIN diode on the top of the upper substrate. A perfect electric conductor (PEC) ground is attached to the bottom of the upper substrate to serve as the ground. A glue layer is used to combine the two substrates, and a biasing circuit is printed on the back of the lower substrate. Both substrates are F4B with the dielectric constant of 2.65 and the loss tangent of 0.001. The thicknesses of the two substrates are 4 and 0.7 mm, respectively. The glue has a dielectric constant of 3.54, a loss tangent of 0.001, and a thickness of 0.1 mm. A PIN diode (Skyworks SMP1320-040LF) [52] is chosen in the element design for the excellent broadband property. When the biasing voltage is above 0.7 V, the PIN diode is switched on and behaves like a small resistor. On the contrary, when the biasing voltage falls to 0 V, the diode is switched off like a capacitor to isolate the DC current. The left patch is connected to the PEC ground, while the right patch is connected to the bottom biasing circuit. The mender lines are used to filter RF signal. The diameter of the metallic vias is 0.4 mm, and the mender lines have a width of 0.2 mm.

The commercial software CST Microwave Studio 2019 is used to investigate the reflection spectrum of the metaatom under different working states of the PIN diode. During the simulation, the unit-cell boundaries are applied in both the x and y directions to incorporate the mutual coupling effect between adjacent elements. Two Floquet ports for x-polarized waves are applied in the $+z$ and $-z$ directions.

The simulated reflection amplitudes/phases and the corresponding far-field scattering patterns are given in Figs. 2(d) and 2(e), respectively. When the PIN diode is turned from on to off, the phase difference is approximately 180° from 6.5 to 8.5 GHz, and the corresponding amplitudes are over 0.9, which means the element can work in both the 0 and 1 states under different biasing voltages. No matter the PIN diode is switched on or off, the scattering wave from the metaatom under normal incidence is always restricted on both sides of the normal direction as illustrated in Fig. 3(e), and the total scattering waves from the metasurface are the superposition of those from the composing elements. Therefore, it is easy to find that the field intensity along the normal direction of the metasurface is the largest.

To illustrate the independent manipulations of the EM waves at both the fundamental and higher-order harmonics, a space-time digital metasurface is encoded to realize the two symmetric beams at the fundamental frequency, and an OAM beam at the ±1st order harmonics. Here, we need to remark that if we want to get an OAM beam with the topological number $l = +1$ for the 1st order harmonic, another OAM beam with the topological number $l = -1$ is also achieved at the −1st order harmonic, which can be explained from Eq. (5). When the initial phase φ_A and the parameter φ_{pq}^{*k} are fixed, it will cause different influences on the ±1st order harmonics by changing the time delay t_1. In other words, if the time delay t_1 is increased, the −1 st harmonic phase is increased as well, while the 1st harmonic phase is decreased with the same degree, giving rise to the opposite topological number as a result.

The space-time digital metasurface consists of 24×24 metaatoms, which are specifically divided into the eight regions [marked from $1^{\#}$ to $8^{\#}$, in Fig. 4(a)] with the same coding sequences Γ_m, but different combination values $(\omega_0 t_1, \varphi_A)$. For the fixed coding sequences Γ_m 000011111111, φ_{pq}^{*k} can be calculated as 180°, 60°, and −60° for the 0th, −1st and 1st order harmonics, respectively, from Eq. (3) and Fig. 2(a). From Eq. (5), the phase at the fundamental frequency can be adjusted by the initial phase φ_A, and the different harmonic phases can be obtained by changing the time delay t_1 at the ±1st order harmonics.

As shown in Fig. 4(a), to achieve two split beams [19–21] at the fundamental frequency, the element phases φ_{pq}^0 are 0° in the left half part (regions $1^{\#}–4^{\#}$), but 180° in the right half (regions $5^{\#}–8^{\#}$). In addition, to realize an OAM beam with the topological number $l = 1$ at the 1st order harmonic, the phase distribution of φ_{pq}^1 is shown in Fig. 4(a), which is gradually increased by a step of 45° from region $1^{\#}$ to the region $8^{\#}$. Substituting φ_{pq}^0, φ_{pq}^1, φ_{pq}^{*0}, φ_{pq}^{*1}, and φ_{pq}^{*-1} into Eq. (5), the values of $\omega_0 t_1$ and φ_{pq}^{-1} in the eight regions are obtained, as listed in Table 1. Note that the phase profile of the −1st order harmonic is just opposite to that of the 1st order harmonic, as demonstrated in Table 1, leading to the OAM beams with the opposite topological numbers.

The far-field scattering pattern of the space-time digital metasurface at the mth order harmonic can be written as [47]
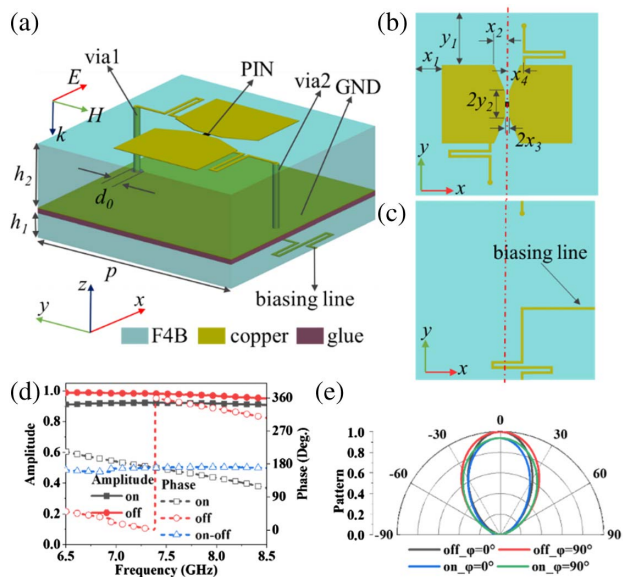

Fig. 3. (a) Perspective view, (b) top view, and (c) bottom view of the metaatom. (d) The simulated reflection spectra of the metaatom under the normal incidence. (e) The scattering patterns of the metaatom for the on and off states. The geometric parameters of the metaatom are $p = 14$, $h_1 = 0.8$, $h_2 = 4$, $d_0 = 0.7$, $x_1 = 2$, $y_1 = 4$, $x_2 = 0.4$, $y_2 = 0.6$, $x_3 = 0.15$, and $x_4 = 0.8$ mm.
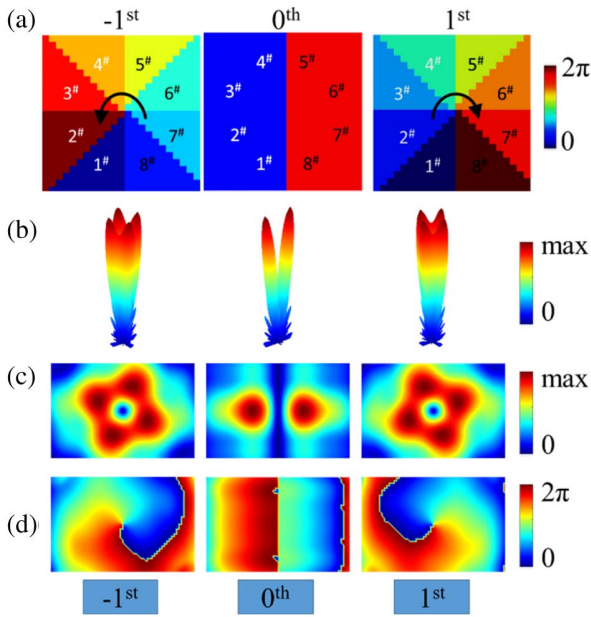
Fig. 4. (a) Required phase distributions of the different harmonics. (b) The corresponding far-field scattering patterns. (c), (d) Near-field amplitude and phase distributions for the −1st, 0th, and 1st order harmonics.

$$F_m(\theta,\varphi) = \sum_{p=1}^{N} \sum_{q=1}^{M} c_{pq}^m E_{pq}(\theta,\varphi) \exp\left(j\frac{2\pi}{\lambda_c}\right)$$
$$\cdot \exp[(p-1)d_x \sin\theta\cos\varphi + (q-1)d_y \sin\theta\sin\varphi],$$
$$\text{(6)}$$

where $E_{pq}(\theta,\varphi)$ is the far-field scattering pattern of the element (p,q) at the fundamental frequency. θ and φ are the elevation and azimuth angles, respectively. d_x and d_y are the element periods along the x and y directions, respectively. λ_c is the wavelength of the fundamental frequency. c_{pq}^m is the complex Fourier coefficient of the periodic reflectivity $\Gamma_{pq}(t)$ at the mth order harmonic. In the ideal theoretical model, the mutual coupling between the coding elements is ignored, and the coding elements are isotropic [i.e., $E_{pq}(\theta,\varphi)=1$]. The fundamental and modulation frequencies are $f_c = 7$ GHz and $f_0 = 10$ kHz, respectively.

Table 1. Combination Values ($\omega_0 t_1$, φ_A) and Calculated Harmonic Phases in the Eight Zones of the Metasurface

Region Number	φ_A (deg)	$\omega_0 t_1$ (deg)	−1st (deg)	0th (deg)	1st (deg)
1#	0	315	15	180	−15
2#	0	270	−30	180	30
3#	0	225	−75	180	75
4#	0	180	−120	180	120
5#	180	315	−165	0	165
6#	180	270	150	0	−150
7#	180	225	105	0	−105
8#	180	180	60	0	−60

From the phase distributions listed in Table 1, the far-field scattering patterns under normal incidence are calculated by Eq. (6) for the different harmonics, as shown in Fig. 4(b). In Fig. 4(b), two symmetric beams at the fundamental frequency, and the vortex beams with hollow intensity at the ±1st order harmonics are generated. To show more details of the harmonic wavefronts, the near-field distributions at the observation plane (located at 1200 mm in front of the metasurface) are calculated and shown in Figs. 4(c) and 4(d). Typical intensity profiles with a hollow center, and spiral phase profiles with different rotation directions can be clearly recognized at the ±1st order harmonics. Besides this, the characteristics of dual beams at the fundamental frequency can also be observed. The calculated profiles for both far and near fields again demonstrate the great potential of the metasurface for nonlinear wavefront controls.

3. EXPERIMENT AND DISCUSSION

To validate the theoretical model, the proposed space-time digital metasurface is fabricated as shown in Figs. 5(a) and 5(b), which is divided into eight regions. The biasing voltages of the eight regions are independently supplied, where the metaatoms in each region share the same voltage during the experiment. An FPGA control board (Artix-7) is employed to provide dynamic biasing voltages for the PIN diodes of the metaatoms. At first, the reflection coefficients of the metasurface are measured via the vector network analyzer (VNA, Agilent N5230C) in an anechoic chamber.

In the first experiment, all the metaatoms are turned on or off simultaneously to measure the reflection amplitudes and phases of 0 and 1 states, as shown in Fig. 5(c). At 7 GHz, the measured amplitudes and phases of the metasurface are approximately 0.7 and 100°, and 0.84 and 260° for the on and off states of the PIN diodes, respectively. The measured phase
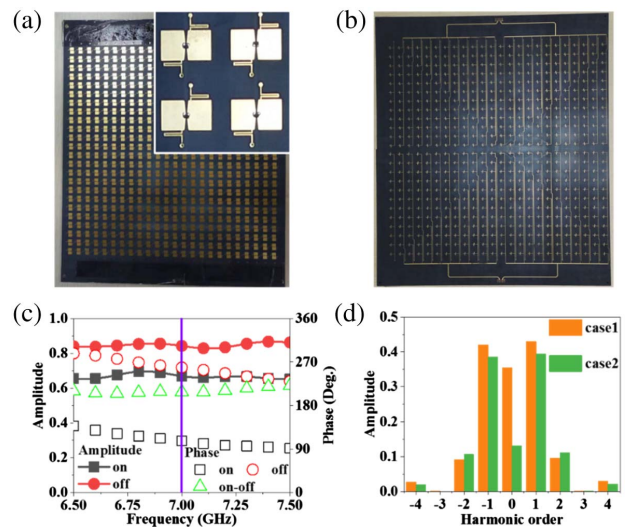

Fig. 5. (a) Front view and (b) back view of the proposed space-time digital coding metasurface. (c) Measured reflection spectra for the on and off states of the PIN diodes. (d) Measured harmonic amplitude distributions under two coding sequences 111100000000 and 000011111111, respectively.

difference between the two states is 200°, which is slightly greater than the desired 180° in theory.

In the second experiment, the reflection spectra under the periodic phase modulation are measured, where two standard horn antennas are employed to transmit and receive signals. One antenna is connected to a microwave signal generator (Keysight E8267D), which provides the excitation signal at 7 GHz. Another horn antenna is used to receive the harmonic scattered signals via a spectrum analyzer (Keysight E4447A). The control circuit is programmed to generate square-wave control signals with the desired biasing voltages, periods, and time delays. The modulation period T of the coding sequences is 100 μs with the modulation frequency $f_0 = 10$ kHz.

Two cases are considered in the experiment, in which the basic coding sequence is 000011111111. The initial phase φ_A is selected as 0° for the case 1, and 180° for the case 2, leading to the changed coding sequence 111100000000 in the case 2. The measured amplitude spectra in the two cases are shown in Fig. 5(d). From Eq. (2), the amplitude spectra should not be affected by the change of φ_A. In Fig. 5(d), the harmonic amplitudes are nearly equal except at the fundamental frequency. This can be ascribed to phase deviations of the metaatoms from their ideal values under different biasing voltages, stemming primarily from the parasitic parameters of the PIN diode, the fabrication tolerance, and the distortion of the control signal.

In the third experiment, the near-field distributions of harmonic waves are monitored with a home-built platform in the microwave anechoic chamber. This is a huge challenge because the traditional mapping apparatus has difficulty acquiring the near fields when the transmitting and receiving frequencies are different. To solve this problem, a novel experimental platform was developed in this work, as depicted in Fig. 6(a). In contrast to the traditional method, two coaxial probes were used to obtain the relative values of the phase and amplitude simultaneously. One was used as the reference probe to provide a reference electric field at the fixed position of the detection plane. The other one can scan the near fields at different positions of the detection plane, whose movement was controlled by a stepping motor. The excitation signal is emitted from a horn antenna connected to the signal generator. Meanwhile, the receiving ends of the two probes are connected to a two-port VNA. Moreover, a phase-locked loop is used to ensure that the VNA and the signal generator are synchronized. The VNA can compare the signals from the two probes. Hence, the near-field distributions can be extracted directly from the amplitude and phase ratios.

The experiment configuration of the nonlinear near field mapping system is shown in Fig. 6(b). The excitation antenna is placed at a distance of 700 mm above the metasurface. The coaxial probe is shown in Fig. 6(c). The scanning plane is located at 1200 mm away from the metasurface, with a scan range of 800 mm × 400 mm (scanning step: 20 mm). The eight regions of the metasurface can be independently controlled by the FPGA control board. The initial coding sequence was 000011111111 with the modulation frequency $f_0 = 10$ kHz, which corresponds to the combination of values $\omega_0 t_1 = 0°$ and $\varphi_A = 0°$. When $\omega_0 t_1 = 0°$ and $\varphi_A = 180°$, the coding sequence is changed to 111100000000.
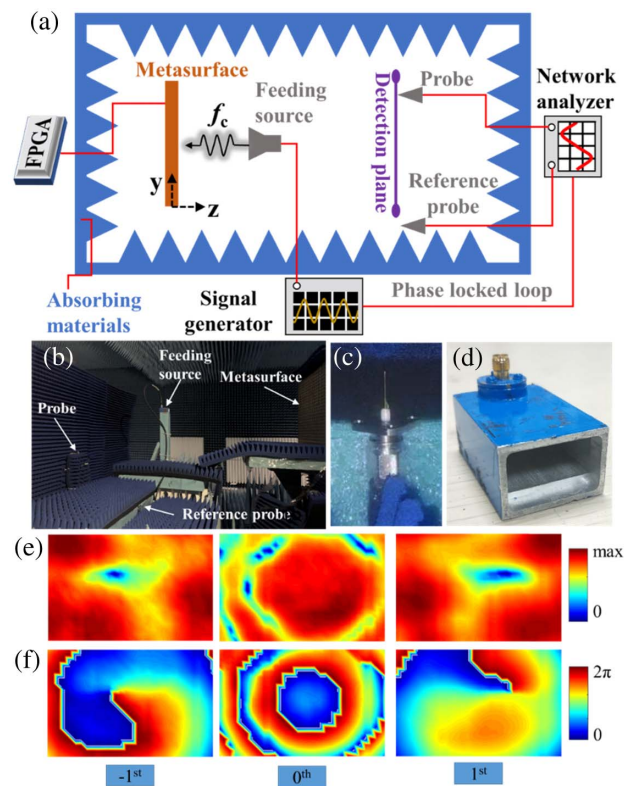

Fig. 6. (a) Schematic of the experimental setup for measuring the harmonic near-field distributions. (b) Photograph of the nonlinear near-field experiment environment. (c) The coaxial probe for near-field detection. (d) The waveguide antenna as the excitation of the metasurface. (e), (f) Measured amplitude and phase distributions of the fundamental and ±1st order harmonics.

Figures 6(e) and 6(f) illustrate the measured harmonic magnitude/phase distributions of the electric fields where φ_A and $\omega_0 t_1$ are listed in Table 1. As expected by the theoretical analysis, the typical intensity profiles with a hollow center, and the spiral phase profiles with different rotation directions can be clearly observed in Figs. 6(e) and 6(f), indicating the generation of OAM beams with the topological number $l = \pm 1$ for ±1st order harmonics. The measured distributions at fundamental frequency are different from the calculated results, which can be ascribed to the huge gap of intensity between the case 1 and case 2 in Fig. 5(d).

There are two main factors responsible for the deviation between the calculated and measured results. (1) The calculated near-field patterns in Figs. 4(c) and 4(d) are obtained under the incidence of plane wave, and the harmonic phases along the metasurface can be accurately determined. However, in the experiment, the feeding source is a waveguide antenna, and it is not a strictly plane wave when arriving at the metasurface. Therefore, the harmonic phase profile is disturbed which may cause the opposite influence on the generations of OAM beams at different harmonics. (2) The measurement of harmonic amplitudes and phases is a great challenge in our experiment. First, the harmonic amplitudes are minimal, and they cannot be directly measured by the VNA. The amplitude/phase comparison method is adopted to solve this

problem where a comparing probe is introduced near the detection plane. The coaxial probe with omnidirectional pattern has low efficiency to obtain the harmonic energies. Besides, the slight vibration of the probe during the movement can also affect the measurement accuracy. (3) Other factors, including parasitic parameters of the PIN diodes, the distortions of the control signals, the fabrication tolerances can also lead to the deviations of the harmonic intensities and phase distributions under the time-varying reflectivity. Nevertheless, from the measured and simulated results, we can still conclude that the time-domain metasurface can manipulate the wavefronts at the fundamental and high-order harmonics independently.

4. CONCLUSIONS

In this paper, we propose a space-time digital metasurface to realize near-field manipulations of the fundamental and $\pm$1st order harmonics. Under the normal incidence of a plane wave, the metasurface can generate two symmetric beams at fundamental frequency, and two OAM beams with the topological number $l = \pm 1$ at the $\pm$1st order harmonics simultaneously. A novel experimental platform for nonlinear field mapping is developed to measure the harmonic near fields of the space-time digital metasurface. Although our experiments are conducted at microwave frequencies, the approach can be further extended into the THz and visible regimes by incorporating advanced modulation technologies.

Disclosures. The authors declare no conflicts of interest.

†These authors contributed equally to this work.

REFERENCES

1. J. B. Pendry, "Negative refraction makes a perfect lens," Phys. Rev. Lett. **85**, 3966–3969 (2000).
2. J. Valentine, S. Zhang, T. Zentgraf, E. Ulin-Avila, D. A. Genov, G. Bartal, and X. Zhang, "Three-dimensional optical metamaterial with a negative refractive index," Nature **455**, 376–379 (2008).
3. G. Rosenblatt and O. Meir, "Perfect lensing by a single interface: defying loss and bandwidth limitations of metamaterials," Phys. Rev. Lett. **115**, 195504 (2015).
4. J. B. Pendry, D. Schurig, and D. R. Smith, "Controlling electromagnetic fields," Science **312**, 1780–1782 (2006).
5. R. Liu, C. Ji, J. J. Mock, J. Y. Chin, T. J. Cui, and D. R. Smith, "Broadband ground-plane cloak," Science **323**, 366–369 (2009).
6. H. F. Ma and T. J. Cui, "Three-dimensional broadband and broad-angle transformation-optics lens," Nat. Commun. **1**, 124 (2010).
7. J. Zhao, Q. Cheng, X. K. Wang, M. J. Yuan, X. Zhou, X. J. Fu, M. Q. Qi, S. Liu, H. B. Chen, Y. Zhang, and T. J. Cui, "Controlling the bandwidth of terahertz low-scattering metasurfaces," Adv. Opt. Mater. **4**, 1773–1779 (2016).
8. L. X. Liu, X. Q. Zhang, M. Kenney, X. Q. Su, N. N. Xu, C. M. Ouyang, Y. L. Shi, J. G. Han, W. L. Zhang, and S. Zhang, "Broadband metasurfaces with simultaneous control of phase and amplitude," Adv. Mater. **26**, 5031–5036 (2014).
9. J. Ding, S. S. An, B. W. Zhang, and H. L. Zhang, "Multiwavelength metasurfaces based on single-layer dual-wavelength meta-atoms:

10. toward complete phase and amplitude modulations at two wavelengths," Adv. Opt. Mater. **5**, 1700079 (2017).
11. N. F. Yu, P. Genevet, M. A. Kats, F. Aieta, J. P. Tetienne, F. Capasso, and Z. Gaburro, "Light propagation with phase discontinuities: generalized laws of reflection and refraction," Science **334**, 333–337 (2011).
12. F. Ding, R. Deshpande, and S. I. Bozhevolnyi, "Bifunctional gap-plasmon metasurfaces for visible light: polarization-controlled unidirectional surface plasmon excitation and beam steering at normal incidence," Light Sci. Appl. **7**, 17178 (2018).
13. H. L. Zhu, S. W. Cheung, K. L. Chung, and T. I. Yuk, "Linear-to-circular polarization conversion using metasurface," IEEE Trans. Antennas Propag. **61**, 4615–4623 (2013).
14. A. Y. Horie, M. Bagheri, and A. Faraon, "Dielectric metasurfaces for complete control of phase and polarization with subwavelength spatial resolution and high transmission," Nat. Nanotechnol. **10**, 937–943 (2015).
15. J. P. B. Mueller, N. A. Rubin, R. C. Devlin, B. Groever, and F. Capasso, "Metasurface polarization optics: independent phase control of arbitrary orthogonal states of polarization," Phys. Rev. Lett. **118**, 113901 (2017).
16. D. W. Hu, J. Cao, W. Li, C. Zhang, T. L. Wu, Q. F. Li, Z. H. Chen, Y. L. Wang, and J. G. Guan, "Optically transparent broadband microwave absorption metamaterial by standing-up closed-ring resonators," Adv. Opt. Mater. **5**, 1700109 (2017).
17. J. Zhao, C. Zhang, Q. Cheng, J. Yang, and T. J. Cui, "An optically transparent metasurface for broadband microwave antireflection," Appl. Phys. Lett. **112**, 073504 (2018).
18. D. Hu, X. Wang, S. Feng, J. Ye, W. Sun, Q. Kan, P. J. Klar, and Y. Zhang, "Ultrathin terahertz planar elements," Adv. Opt. Mater. **1**, 186–191 (2013).
19. L. L. Huang, X. Z. Chen, H. Mühlenbernd, H. Zhang, S. M. Chen, B. F. Bai, Q. F. Tan, G. F. Jin, K. W. Cheah, C. W. Qiu, J. S. Li, T. Zentgraf, and S. Zhang, "Three-dimensional optical holography using a plasmonic metasurface," Nat. Commun. **4**, 2808 (2013).
20. L. H. Gao, Q. Cheng, J. Yang, S. J. Ma, J. Zhao, S. Liu, H. B. Chen, Q. He, W. X. Jiang, H. F. Ma, Q. Y. Wen, L. J. Liang, B. B. Jin, W. W. Liu, L. Zhou, J. Q. Yao, P. H. Wu, and T. J. Cui, "Broadband diffusion of terahertz waves by multi-bit coding metasurfaces," Light Sci. Appl. **4**, e324 (2015).
21. C. D. Giovampaola and N. Engheta, "Digital metamaterials," Nat. Mater. **13**, 1115–1121 (2014).
22. T. J. Cui, M. Q. Qi, X. Wan, J. Zhao, and Q. Cheng, "Coding metamaterials, digital metamaterials and programmable metamaterials," Light Sci. Appl. **3**, e218 (2014).
23. X. Wan, X. P. Shen, Y. Luo, and T. J. Cui, "Planar bifunctional Luneburg-fisheye lens made of an anisotropic metasurface," Laser Photon. Rev. **8**, 757–765 (2014).
24. M. Khorasaninejad, F. Aieta, P. Kanhaiya, M. A. Kats, P. Genevet, D. Rousso, and F. Capasso, "Achromatic metasurface lens at telecommunication wavelengths," Nano Lett. **15**, 5358–5362 (2015).
25. J. Yang, C. Zhang, H. F. Ma, J. Zhao, J. D. Dai, W. Yuan, L. X. Yang, Q. Cheng, and T. J. Cui, "Generation of radio vortex beams with designable polarization using anisotropic frequency selective surface," Appl. Phys. Lett. **112**, 203501 (2018).
26. L. L. Li, T. Jun Cui, W. Ji, S. Liu, J. Ding, X. Wan, Y. Bo Li, M. Jiang, C. W. Qiu, and S. Zhang, "Electromagnetic reprogrammable coding-metasurface holograms," Nat. Commun. **8**, 197 (2017).
27. J. Yang, C. Zhang, H. F. Ma, W. Yuan, L. X. Yang, J. C. Ke, M. Z. Chen, A. Mahmoud, Q. Cheng, and T. J. Cui, "Tailoring polarization states of multiple beams that carry different topological charges of orbital angular momentums," Opt. Express **26**, 31664–31674 (2018).
28. X. Ni, A. V. Kildishev, and V. M. Shalaev, "Metasurface holograms for visible light," Nat. Commun. **4**, 2807 (2013).
29. J. W. Wu, Z. X. Wang, Z. Q. Fang, J. C. Liang, X. Fu, J. F. Liu, H. T. Wu, D. Bao, L. Miao, X. Y. Zhou, Q. Cheng, and T. J. Cui, "Full-state synthesis of electromagnetic fields using high efficiency phase-only metasurfaces," Adv. Funct. Mater. **30**, 2004144 (2020).
30. J. W. Wu, R. Y. Wu, X. C. Bo, X. J. Fu, and T. J. Cui, "Synthesis algorithm for near-field power pattern control and its experimental verification via metasurfaces," IEEE Trans. Antennas Propag. **67**, 1073–1083 (2019).

30. J. W. Wu, Z. X. Wang, Q. Cheng, and T. J. Cui, "Anisotropic metasur-face holography in 3D space with high resolution and efficiency," IEEE Trans. Antennas Propag. **69**, 302–316 (2021).

31. T. J. Cui, S. Liu, G. D. Bai, and Q. Ma, "Direct transmission of digital message via programmable coding metasurface," Research **2019**, 2584509 (2019).

32. Z. Tao, X. Wan, B. C. Pan, and T. J. Cui, "Reconfigurable conversions of reflection, transmission, and polarization states using active meta-surface," Appl. Phys. Lett. **110**, 121901 (2017).

33. C. Zhang, J. Gao, X. Cao, S. J. Li, H. H. Yang, and L. Li, "Multifunction tunable metasurface for entire-space electromagnetic wave manipu-lation," IEEE Trans. Antennas Propag. **68**, 3301–3306 (2020).

34. C. Huang, C. L. Zhang, J. Yang, B. Sun, B. Zhao, and X. G. Luo, "Reconfigurable metasurface for multifunctional control of electromag-netic waves," Adv. Opt. Mater. **5**, 1700485 (2017).

35. M. Qian, G. D. Bai, H. B. Jing, C. Yang, L. L. Li, and T. J. Cui, "Smart metasurface with self-adaptively reprogrammable functions," Light Sci. Appl. **8**, 98 (2019).

36. J. Zhao, Q. Cheng, J. Chen, M. Q. Qi, W. X. Jiang, and T. J. Cui, "A tunable metamaterial absorber using varactor diodes," New J. Phys. **15**, 043049 (2013).

37. Z. J. Luo, Q. Wang, X. G. Zhang, J. W. Wu, J. Y. Dai, L. Zhang, H. T. Wu, H. C. Zhang, H. F. Ma, Q. Cheng, and T. J. Cui, "Intensity-depen-dent metasurface with digitally reconfigurable distribution of nonline-arity," Adv. Opt. Mater. **7**, 1900792 (2019).

38. Z. J. Luo, M. Z. Chen, Z. X. Wang, L. Zhou, Y. B. Li, Q. Cheng, H. F. Ma, and T. J. Cui, "Digital nonlinear metasurface with customizable nonreciprocity," Adv. Funct. Mater. **29**, 1906635 (2019).

39. G. X. Zhang, W. X. Tang, W. X. Jiang, G. D. Bai, J. Tang, L. Bai, C. W. Qiu, and T. J. Cui, "Light-controllable digital coding metasurfaces," Adv. Sci. **5**, 1801028 (2018).

40. S. V. Hum and J. Carrier, "Reconfigurable reflectarrays and array lenses for dynamic antenna beam control: a review," IEEE Trans. Antennas Propag. **62**, 183–198 (2014).

41. M. Kauranen and A. V. Zayats, "Nonlinear plasmonics," Nat. Photonics **6**, 737–748 (2012).

42. A. E. Minovich, A. E. Miroshnichenko, A. Y. Bykov, T. V. Murzina, D. N. Neshev, and Y. S. Kivshar, "Functional and nonlinear optical meta-surfaces," Laser Photon. Rev. **9**, 195–213 (2015).

43. G. Li, S. Chen, N. Pholchai, B. Reineke, P. W. H. Wong, E. Y. B. Pun, K. W. Cheah, T. Zentgraf, and S. Zhang, "Continuous control of the nonlinearity phase for harmonic generations," Nat. Mater. **14**, 607–612 (2015).

44. E. Almeida, G. Shalem, and Y. Prior, "Subwavelength nonlinear phase control and anomalous phase matching in plasmonic metasurfaces," Nat. Commun. **7**, 10367 (2016).

45. G. Li, S. Zhang, and T. Zentgraf, "Nonlinear photonic metasurfaces," Nat. Rev. Mater. **2**, 17010 (2017).

46. J. Zhao, X. Yang, J. Y. Dai, Q. Cheng, X. Li, N. H. Qi, J. C. Ke, G. D. Bai, S. Liu, S. Jin, A. Alu, and T. J. Cui, "Programmable time-domain digital-coding metasurface for non-linear harmonic manipulation and new wireless communication systems," Natl. Sci. Rev. **6**, 231–238 (2018).

47. L. Zhang, X. Q. Chen, S. Liu, Q. Zhang, J. Zhao, J. Y. Dai, G. D. Bai, X. Wan, Q. Cheng, G. Castaldi, V. Galdi, and T. J. Cui, "Space-time-cod-ing digital metasurfaces," Nat. Commun. **9**, 4334 (2018).

48. L. Zhang, X. Q. Chen, R. W. Shao, J. Y. Dai, Q. Cheng, G. Castaldi, V. Galdi, and T. J. Cui, "Breaking reciprocity with space-time-coding dig-ital metasurfaces," Adv. Mater. **31**, 1904069 (2019).

49. J. Y. Dai, J. Zhao, Q. Cheng, and T. J. Cui, "Independent control of harmonic amplitudes and phases via a time-domain digital coding metasurface," Light Sci. Appl. **7**, 90 (2018).

50. J. C. Ke, J. Y. Dai, M. Z. Chen, L. Wang, C. Zhang, W. Tang, J. Yang, W. Liu, X. Li, Y. F. Liu, Q. Cheng, S. Jin, and T. J. Cui, "Linear and nonlinear polarization syntheses and their programmable controls based on anisotropic time-domain digital coding metasurface," Small Struct. **2**, 2000060 (2021).

51. J. Y. Dai, J. Yang, W. Tang, M. Z. Chen, J. C. Ke, Q. Cheng, S. Jin, and T. J. Cui, "Arbitrary manipulations of dual harmonics and their wave behaviors based on space-time-coding digital metasurface," Appl. Phys. Rev. **7**, 041408 (2020).

52. https://www.skyworksinc.com.